

Calibrated Microwave Reflectance in Low-Temperature Scanning Tunneling Microscopy

Bareld Wit^{1,a)}, Georg Gramse², and Stefan Müllegger¹

Affiliations

- 1 Institute of Semiconductor and Solid State Physics, Johannes Kepler University Linz, 4040 Linz, Austria
- 2 Biophysics Institute, Johannes Kepler University, 4020 Linz, Austria

a) Author to whom correspondence should be addressed: bareld.wit@jku.at

Abstract

We outline calibrated measurements of the microwave reflection coefficient from the tunnel junction of an ultra-high vacuum low temperature scanning tunneling microscope. The microwave circuit design, including an interferometer set-up for enhanced signal-to-noise and a demodulation scheme for lock-in detection, is described in detail. A quantitative, *in-situ* procedure for impedance calibration based on the numerical 3-error-term model is presented. Our procedure exploits the response of the microwave reflection signal due to the change of the tunneling conductance caused by sub-nm variation of the tunneling distance. Experimental calibration is achieved by a least-squares numerical fit of simultaneously measured conductance and microwave reflection retraction curves at finite conductance. Our method paves the way for nanoscale microscopy and spectroscopy of dielectric surface properties at GHz frequencies and cryogenic temperatures. This opens a promising pathway even for dielectric fingerprinting at the single molecule limit.

Introduction

Recent developments of near-field scanning microwave microscopy¹ have enabled the characterization of materials with nanoscale dimensions, surfaces, and nanoelectronics devices² up to GHz frequencies and with sub-micron lateral resolution. In particular, this includes measuring electrostatic force^{3,4}, electrical capacitance^{5,6} and electrochemical activity⁷. Each of these techniques has its specific limitations like the frequency of operation^{6,8,9}. Recently, microwave reflection spectroscopy with sub-micron lateral resolution has been demonstrated up to 19 GHz^{10,11}. Various material properties, including relative dielectric permittivity¹² and dopant concentration² have been successfully detected by a transmission line implementation realized in an atomic force microscope operated at ambient conditions. Although closely related to the atomic force microscope, the scanning tunneling microscope (STM) has been scarcely demonstrated as platform for calibrated microwave reflection spectroscopy to date. The present work outlines a straightforward approach, *i.e.* utilizing the STM tip as a probe for calibrated microwave reflection spectroscopy. In particular, we employ a low-temperature STM instrument, which is well-known to provide ultimate stability and spatial resolution¹³ by operating at ultra-high vacuum conditions and cryogenic temperatures. Our approach offers great potential for achieving microwave impedance spectroscopic fingerprinting even at the

scale of single molecules – thus complementing related methods that utilize spin-resonance^{14,15} or dielectric relaxation¹⁶ at GHz frequencies.

Commonly, the tunnel junction of an STM exhibits an impedance Z_{jun} of 10^8 to $10^9 \Omega$. In contrast, the impedance of the microwave transmission line built from standard microwave components is $Z_{\text{ref}} = 50 \Omega$. The interface of the tunnel junction to the microwave transmission line thus represents a massive change of impedance, which affects the degree of reflection of an incoming microwave at the junction. The latter is described by the complex-valued scattering parameter¹⁷

$$S_{11,\text{jun}} = \frac{Z_{\text{jun}} - Z_{\text{ref}}}{Z_{\text{jun}} + Z_{\text{ref}}} \quad (1)$$

Accordingly, the STM junction will almost completely reflect incoming microwaves, *i.e.* $S_{11} \approx 1$. Notice that S_{11} is frequency-dependent, since the complex impedance of the tunnel junction depends on the frequency f of the microwave as well as on the conductance G and capacitance C of the junction¹⁷

$$Z_{\text{jun}} = \frac{1}{Y_{\text{jun}}} = \frac{1}{G + i 2\pi f C} \quad (2)$$

where Y_{jun} is the complex-valued admittance and $i = \sqrt{-1}$ is the imaginary unit. Setting well-defined values for Z_{ref} and f leaves S_{11} dependent on G and C of the junction only. This dependency lies at the heart of microwave reflectance spectroscopy implemented on a scanning probe instrument^{18,19}, relying on the accurate quantitative determination of C from measured S_{11} data. Such quantitative determination requires accurate calibration, because $S_{11,\text{jun}}$ cannot be measured directly. Instead, the experimental measurement yields the reflection coefficient $S_{11,\text{m}} \neq S_{11,\text{jun}}$. Notice that the subscript m indicates that S_{11} is measured at a point far away from the junction, *i.e.* after the reflected microwave has travelled back through various circuit components of the transmission line. The amplitude and phase of the complex-valued $S_{11,\text{m}}$ systematically deviate from $S_{11,\text{jun}}$ due to microwave absorptions and reflections in the transmission line. According to the well-known numerical 3-error-term model^{10,20}, the relation between $S_{11,\text{jun}}$ and $S_{11,\text{m}}$ is described by three complex-valued parameters e_{00} , e_{01} , and e_{11}

$$S_{11,\text{m}} = e_{00} + e_{01} \frac{S_{11,\text{jun}}}{1 - e_{11} S_{11,\text{jun}}} \quad (3)$$

Importantly, the S_{11} phase and amplitude depend strongly on the exact frequency chosen. Therefore, the e -parameters have to be determined separately for every measurement frequency.

In this work, we present a retraction calibration procedure that uses simultaneous $G(z)$ and $S_{11}(z)$ measurements upon the well-controlled variation of the tunnel distance z . We determine the numerical values of the e -parameters of Eq. (3) that define the calibration. Additionally, we present our implementation of microwave reflection spectroscopy in a low-temperature ultra-high vacuum STM. Our STM instrument has been upgraded by a cryogenic microwave transmission line^{20,21}. The microwave circuit design described herein incorporates a custom interferometer and lock-in detection, forgoing the use of a vector network analyzer.

Methods

Microwave reflectance measurements were performed on our upgraded Createc low-temperature ultra-high vacuum STM system ($p < 4 \cdot 10^{-11}$ mbar, $T < 8.5$ K)^{21,22}. All experiments herein were performed over a clean Au(111) surface (Surface preparation laboratory), prepared by repeated cycles of Ar ion sputtering (0.61 kV, 10 min) and annealing (703 K, 10 min). A tungsten tip (Bruker DTT10) was used as the STM and microwave probe. The bias voltage V_{DC} was applied to the tip. The

microwave signal was added to V_{DC} via a bias-tee (SHF BT45R-B). Inside the vacuum chamber, the microwaves are transmitted via microwave compatible cables (Elspec MK5001 and Elspec Stormflex 047Cryo). At the sample side, a second bias-tee (Tektronix PSPL5541A) separates the DC line, which is grounded at the tunnel current amplifier (Femto DLPCA 200), and the microwave line, which is terminated with a 50Ω load.

We detect amplitude changes and phase shifts of the microwaves that have been reflected at the tunnel junction. In order to increase the signal-to-noise ratio, the background resulting from the near full microwave reflection at the tunnel junction [see Eq. (1)] was subtracted using a Mach-Zehnder type interferometer¹¹. The orange shaded section of the schematic in Fig. 1 depicts the components and layout of the interferometer. Table I lists the details of the indicated components. The transmission line to the STM tip acts as the measurement signal of the interferometer (see pink arrows in Fig. 1), while the variable voltage attenuator (VVA) acts as the difference signal (see cyan arrows in Fig. 1). An optimum (*i.e.* highest) signal-to-noise ratio for $S_{11,m}$ detection is achieved for destructive interference between the two paths in the interferometer. This happens when the signals from the two parts have the same amplitude and are antiphase. Amplitude matching is performed by tuning the attenuation of the difference signal by the VVA input voltage. Antiphase conditions are obtained at fixed frequencies where the total path length of the two arms differ by exactly $(n + 1/2) \lambda$, where n is an integer and λ is the microwave wavelength. The frequencies for which this condition is satisfied are referred to as notches in the frequency spectrum¹¹. Calibration measurements are performed at a frequency f and VVA attenuation that maximizes destructive interference in the interferometer at the tunneling setpoint, creating a notch as shown in Fig. 2(a).

The green shaded section of the schematic in Fig. 1 depicts the down-modulation circuit and table I lists the details of the indicated components. Before down-modulation, the microwaves coming from the interferometer are amplified using a low-noise amplifier (LNA). Then, the microwave signal is demodulated to an intermediate frequency f_{IF} , since the microwave frequency f is too high to detect with a lock-in amplifier directly. The demodulated signal was detected using a lock-in amplifier, at a reference frequency of f_{IF} obtained by demodulating a fraction of the microwaves going to the interferometer. With this arrangement, continuous phase stable detection is achieved. In the experiments presented herein, $f = 0.908$ GHz and $f_{IF} = 500$ kHz. The peak-to-peak amplitude of the incident microwaves at the tunnel junction²¹ was determined to be $V_{pp,RF} = 69$ mV. G was measured by a lock-in amplifier (EG&G 5210) using a sinusoidal modulation of V_{DC} ($V_{rms,lock-in} = 8$ mV, $f_{lock-in} = 775$ Hz).

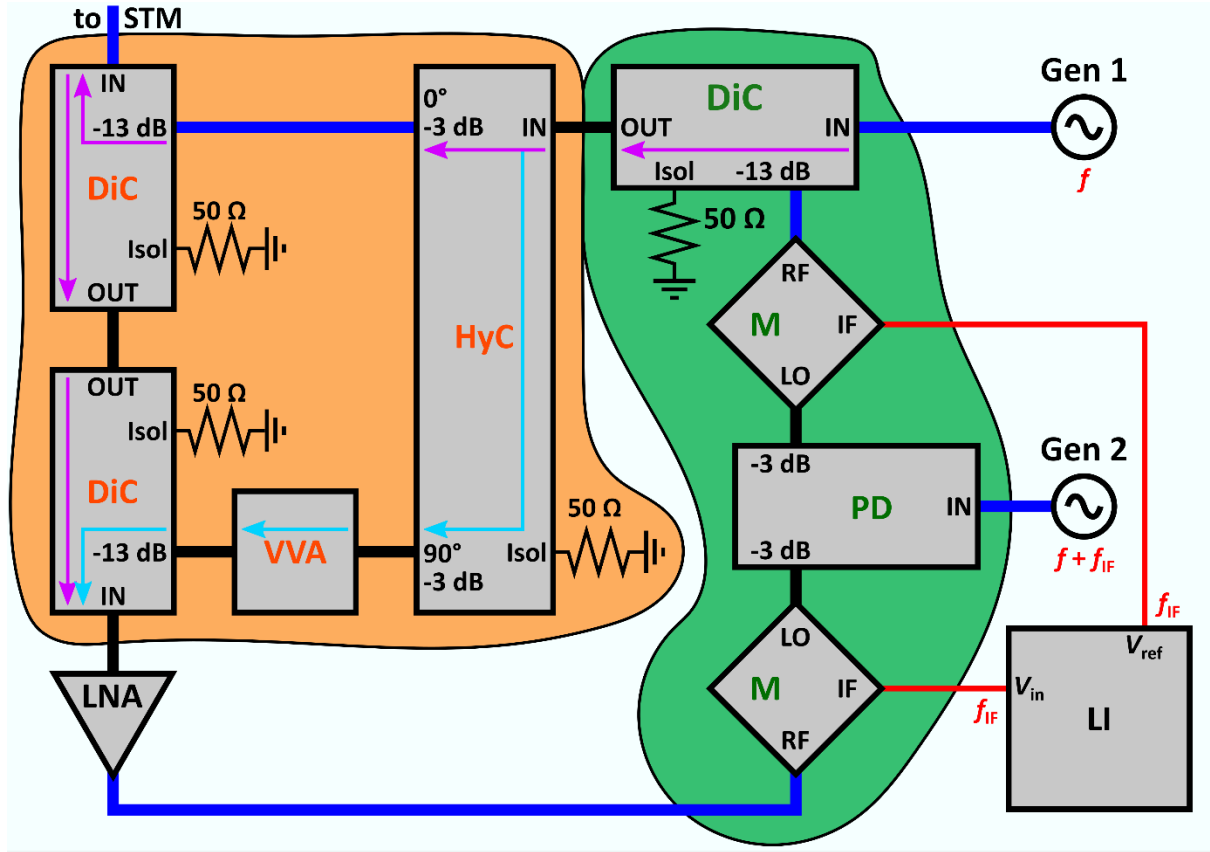


FIG. 1: Block diagram of the interferometer microwave circuit (shaded orange) and the down-conversion section (shaded green). Pink and cyan arrows indicate the measurement and difference paths of the microwaves through the interferometer, respectively. Specific ports of the components are labeled. Black lines indicate connections via a single adapter piece, blue lines are dedicated microwave cables, and red lines are low-noise BNC cables. For details of the components, see Table I.

Table I: Details of the microwave circuit components depicted in Fig. 1.

Label	Component	Brand/type
DiC	Directional Coupler	Marki C13-0126
HyC	Hybrid Coupler	Marki QH0R518
PD	Power Divider	Marki PD0126
M	3-Port Mixer	Mini Circuits ZX05-63LH-S+
LNA	Low-Noise Amplifier	Low Noise Factory LNR1_15A_SV
VVA	Variable Voltage Attenuator	Universal Microwave Corp. AG-U000-60V
Gen 1	Generator 1	Keysight E8257D
Gen 2	Generator 2	Rohde & Schwarz SMA100A
LI	Lock-In Amplifier	Zurich Instruments MFLI

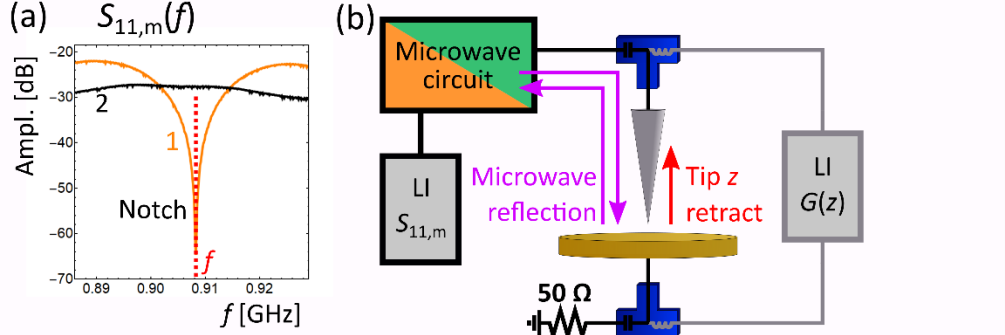


FIG. 2: Details of the retraction curve calibration. (a) Microwave scattering parameter $S_{11,m}(f)$ measured with (orange curve 1) and without (black curve 2) the interferometer. The frequency f where destructive interference in the interferometer is maximized is indicated with a red dashed line. (b) In retraction curve calibration, the tip is retracted from $z = -1$ nm to $z = 50$ nm with respect to the tunneling setpoint represented by $z = 0$ nm. $S_{11,m}(z)$ and conductance $G(z)$ are measured simultaneously during tip retraction. To determine $S_{11,m}(z)$, a microwave signal is added to V_{DC} via a bias tee. The microwaves are reflected at the tunnel junction (purple arrows). The full block diagram of the $S_{11,m}(z)$ detection scheme, labeled Microwave circuit, is shown in Fig. 1. $G(z)$ is measured with a lock-in amplifier using a sinusoidal modulation of V_{DC} , see methods. The rest of the STM electronics are omitted for clarity.

Results

Fig. 2(b) outlines the schematic of our retraction curve measurement for the calibration of S_{11} based on the simultaneous measurement of $G(z)$ and $S_{11,m}(z)$ during tip retraction. Fig. 3(a) shows $G(z)$ recorded while retracting the tip a distance of $\Delta z = 51$ nm away from the Au(111) surface. Prior to recording this retraction curve, the tip was approached by $\Delta z = -1$ nm from the tunneling setpoint (51 pA and 20 mV), representing $z = 0$, to the starting point of the retraction curve at $z = -1$ nm. This was done in order to achieve a sufficiently large change of $S_{11,m}(z)$, which is found to occur at a conductance close to $1 G_0$, while retaining an exponential $G(z)$ relation in the tunneling regime, as shown in the inset of Fig. 3(a). Here, $G_0 = 2 e^2/h \approx 77.48 \mu\text{S}$ is the conductance quantum, $e \approx +1.6022 \cdot 10^{-19} \text{ C}$ is the elementary charge and $h \approx 6.6261 \cdot 10^{-34} \text{ Js}$ is the Planck constant. The red curves in Fig. 3(a) represent a numerical fit to the $G(z)$ curve with an exponential decay function, as is well-established for STM¹³

$$G(z) = e^{-2\kappa(z-z_0)} \quad (4)$$

where κ and z_0 are parameters of the fit.

In our concurrent microwave reflection measurement, the amplitude of $S_{11,m}(z)$ decreases approximately linearly over the entire retraction range as shown in Fig. 3(b). In contrast, the phase of $S_{11,m}(z)$ shows a sharp increase in the first nm above the surface, followed by a nearly linear increase over the rest of the retraction curve. Fig. 3(c) shows the same $S_{11,m}(z)$ data in a different representation, *i.e.* plotted in the complex plane and the z -dependence shown as color gradient. Based on the shape of the $S_{11,m}(z)$ curve we distinguish two different regimes, labeled high G (red marker) and $G = 0$ (cyan marker). The high G regime ranges from $z = -1$ nm to $z \approx -0.8$ nm and is characterized by a conductance of about $G > G_0 / 3$. The $G = 0$ regime starts at $z \approx 4$ nm.

In the next step, the values of the parameters e_{00} , e_{01} , and e_{11} are determined from the experimental $S_{11,m}(z)$ data with the help of a numerical least-squares fit using Eq. (3). We obtain the

values $e_{00} = -1.71 + 0.04 i$, $e_{01} = 0.41 - 2.31 i$, and $e_{11} = 0.91 + 0.79$. Notice that the numerical fit procedure concerns the difference between the experimental data (Fig. 3c) and the respective values predicted by Eq. (3), as follows: The scattering parameter at the tunnel junction $S_{11,\text{jun}}(z)$ is calculated using Eqs. (2) and (1). The exponential fit to $G(z)$ of Eq. (4), as shown in Fig. 3(a), is used for the conductance term in Eq. (2). For the unknown capacitance term, we apply a Taylor series approximation of $C(z) \approx C(d) + C'(d)(z - d) + \dots$. Since we perform the numerical fitting in a narrow z -range of 0.54 nm, we consider only the constant and linear terms of the series and neglect higher terms. Notice that in the high G regime, the exponential decay of $G(z)$ dominates the linear $C'(d)(z - d)$ term in the Taylor expansion of $C(z)$. Therefore, we also neglect the linear term and assume $C(z) = \text{const}$ in Eq. (2) for the rest of our analysis. We remark that after successful calibration the validity of the assumption is confirmed, *i.e.* the z -range of $z = -1$ to -0.46 nm used for calibration is sufficiently narrow (see discussion).

Fig. 3(d) shows our result of the calibration, where the experimental $S_{11,\text{m}}(z)$ data from Fig. 3(c) has been transformed into calibrated admittance $Y_{\text{jun}}(z)$ using the values of the e -parameters obtained from the numerical fit procedure above. Notice that according to Eq. (2), $Y_{\text{jun}}(z) = G + i 2\pi f C$ and thus the real and imaginary parts of $Y_{\text{jun}}(z)$ correspond to G and C , respectively. After calibration the different conduction regimes can still be clearly distinguished [compare Figs. 3(c) and (d)]. As expected, the high G regime (red, $z < -0.8$ nm) is dominated by a change of G , while C remains almost constant. Conversely, the low- G regime (cyan, $z > 4$ nm) is dominated by a significant change of C , while the value of G is almost constant at $G \approx 0$.

Fig. 3(e), upper panel shows the calibrated data of Fig. 3(d) in a different representation, *i.e.* $G^{\text{MW}}(z)$ in the upper panel and $C^{\text{MW}}(z)$ in the lower panel. To avoid confusion with the conventionally obtained G data, the superscript MW indicates that the respective data has been obtained from the microwave reflection procedure.

Discussion

The quality of the obtained calibration can be judged by comparing the conductance data, as shown in Fig. 3(e), that has been obtained in two different manners: Firstly, G directly measured by the common dI/dV lock-in method [red curve, $G(z)$] and, secondly, G obtained from the microwave reflection procedure described above [blue curve, $G^{\text{MW}}(z)$]. As can be seen, both curves are in reasonably good agreement. Notice that the agreement is particularly good in the calibration interval of $z < -0.46$ nm, as illustrated in the inset of the upper panel of Fig. 3(e). From this good quantitative agreement, we conclude that the calibration was successful. We remark that the minor discrepancy between the fit to $G(z)$ (red) and the $G^{\text{MW}}(z)$ data (blue) in the calibration interval cannot be explained by deviations in C due to the tip apex. Instead, it may be rationalized by the frequency dependence of G ^{23,24} that is not explicitly included in the calibration procedure and goes beyond the scope of the present work.

In order to verify the validity of our assumption that the change in capacitance is negligible on the calibration interval of $z = -1$ to -0.46 nm, we compare the relative impact of changes in G and C on $Y_{\text{jun}}(z)$. We obtain a respective change of $\Delta G(z) = \Delta \text{Re}(Y_{\text{jun}}(z)) \approx 1.6 G_0 \approx 126 \mu\text{S}$, see inset of upper panel of Fig. 3(e). In comparison, a linear fit over the whole z -range from -1 to +50 nm of the $\Delta C^{\text{MW}}(z)$ curve, see lower panel of Fig. 3(e), yields a value for the slope $\partial C^{\text{MW}}(z)/\partial z$ of -2.3 fF/nm , resulting in an absolute change of $\Delta C^{\text{MW}} \approx 1.2 \text{ fF}$ over the respective z -range ($\Delta z = 1 - 0.46 = 0.54$ nm), and finally resulting in a value of $\Delta C^{\text{MW}} 2\pi f = \Delta \text{Im}(Y_{\text{jun}}(z)) \approx 7 \mu\text{S}$. This value is circa 20 times smaller (!) than the above value of $126 \mu\text{S}$, demonstrating that Y_{jun} is indeed dominated by G .

(and not by C), in agreement with the above assumption. Notice that within the calibration interval the slope $\partial G(z)/\partial z$ derived from the upper panel of Fig. 3(e) is found to be always larger than the respective slope of $2\pi f \partial C^{\text{MW}}(z)/\partial z$ (see above), which is again in agreement with the above assumption. Repeating the calibration for slightly larger and smaller z -ranges (± 0.05 nm) yields values that are in good agreement (*i.e.* within $<4\%$ deviation) to the above values. Furthermore, either enforcing the $G = 0$ condition for $z > 10$ nm or accounting for the linear term in $C(z)$ in a self-consistent optimization loop, again yields consistent values. This shows that the calibration procedure yields robust values for the capacitance.

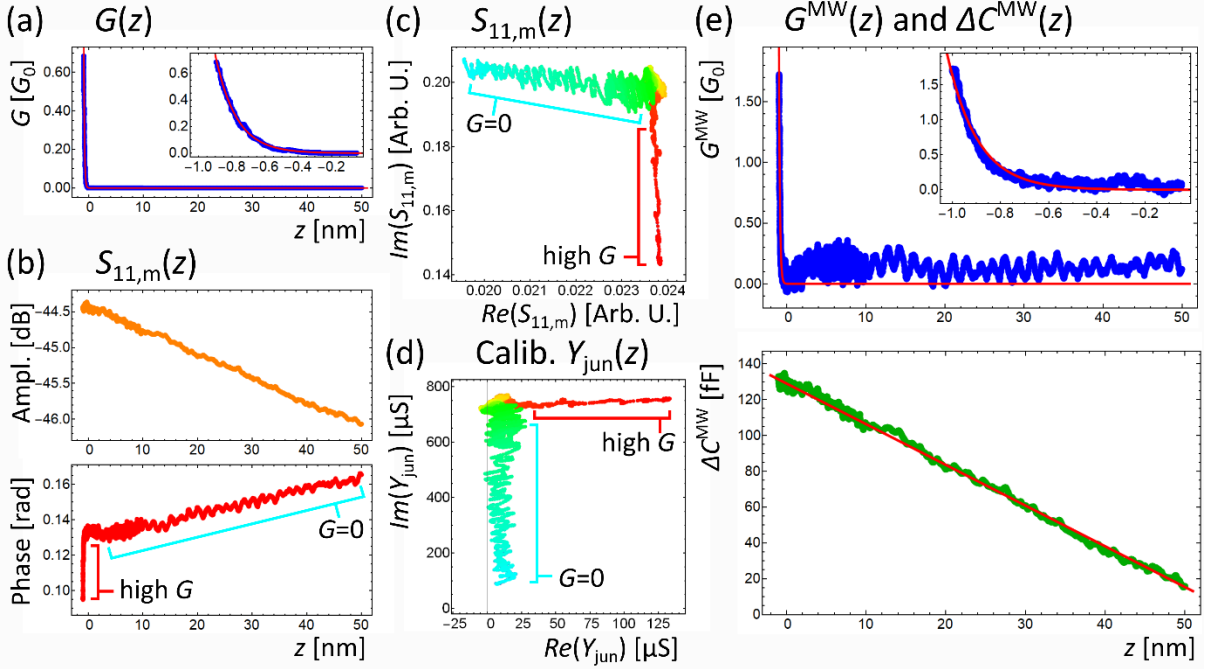


FIG. 3: Experimental retraction curves and the result of calibration. (a) Conductance retraction curve $G(z)$ recorded over clean Au(111). The inset shows the portion of $G(z)$ at $z < 0$. The red curves represent a fit with an exponential decay function ($R^2 = 0.9986$). (b) z -dependence of amplitude (upper panel) and phase (lower panel) of the complex $S_{11,m}(z)$ during the microwave reflection retraction curves. (c) $S_{11,m}$ plotted in the complex plane. The color code is non-linear with respect to z , with red being points taken closest to the surface and green/cyan furthest away from the surface. (d) Calibrated admittance Y_{jun} (reciprocal impedance). (e) The conductance $G^{\text{MW}}(z)$ (upper panel) and capacitance change $\Delta C^{\text{MW}}(z)$ (lower panel) as extracted from the calibrated admittance. The inset in the upper panel shows the portion of $G^{\text{MW}}(z)$ at $z < 0$. The red curves in the upper panel represent the exponential fit function to $G(z)$ from the inset in (a). The red line in the lower panel indicates a linear fit ($R^2 = 0.9957$). All z -values are reported relative to the tunneling setpoint, with negative numbers meaning closer to the surface.

Conclusion

We present a calibration procedure for microwave reflectance spectroscopy based on the acquisition of conductance retraction curves in an ultra-high vacuum low-temperature STM instrument. While the retraction curve calibration concept based on capacitive force detection has been very successfully employed for microwave reflection measurements in an AFM¹⁰ in the past, in STM the force detection

is not available. Therefore, we acquire the tunneling conductance, which changes exponentially with distance, instead of the capacitance, which has a long-range interaction and changes only slowly with tip sample distance. We show that in the high G regime, for approximately $G > G_0/3$ occurring at sub-nm tip-sample distances, the change of the measured scattering parameter $S_{11,m}$ with respect to the tunnel distance is dominated by changes in the conductance signal. In this narrow z-range of 0.54 nm in the high-conduction regime, the change of the junction capacitance with tunnel distance can be neglected. This allows for a successful calibration of the error parameters describing the distortion of $S_{11,m}$ relative to the scattering parameter at the tunnel junction $S_{11,jun}$. We remark that the employed e -parameter procedure captures all non-idealities of the transmission line and detection circuit and can be readily extended to calibration of an entire range of frequencies. The calibration of microwave reflectance spectra presented here will pave the way for quantitative capacitance and dielectric spectroscopy measurements with a lateral resolution of a few nm and ultimately single molecule fingerprinting in low-temperature ultra-high vacuum STM.

Acknowledgments

The authors acknowledge the financial support the European Research Council (ERC) under the European Union's Horizon 2020 research and innovation programme (Grant Agreement No. 771193). This project additionally received funding from EMPIR project 20IND12 Elena.

Author declarations

Conflict of Interest

The authors have no conflicts to disclose.

Author Contributions

Bareld Wit: Conceptualization, Formal Analysis, Methodology, Validation, Visualization, and Writing. Georg Gramse: Conceptualization, Funding Acquisition, Methodology, Validation, and Writing. Stefan Mülegger: Conceptualization, Validation, Funding Acquisition, Project Administration, Supervision, and Writing.

Data availability

The data that support the findings of this study are available from the corresponding author upon reasonable request.

References

- ¹ A. Imtiaz, T. M. Wallis, and P. Kabos, *IEEE Microw. Mag.* **15**, 52 (2014).
- ² H. P. Huber, I. Humer, M. Hochleitner, *et al.*, *J. Appl. Phys.* **111**, 014301 (2012).
- ³ Y. Martin, D. W. Abraham, and H. K. Wickramasinghe, *Appl. Phys. Lett.* **52**, 1103 (1988).
- ⁴ S. Gómez-Moñivas, L. S. Froufe-Pérez, A. J. Caamaño, and J. J. Sáenz, *Appl. Phys. Lett.* **79**, 4048 (2001).
- ⁵ J. R. Matey, and J. Blanc, *J. Appl. Phys.* **57**, 1437 (1985).

⁶ P. J. Hansen, Y. E. Strausser, A. N. Erickson, *et al.*, *Appl. Phys. Lett.* **72**, 2247 (1998).

⁷ S. Grall, I. Alić, E. Pavoni, *et al.*, *Small* **17**, 2101253 (2021)

⁸ C. Gao, T. Wei, F. Duewer, Y. Lu, and X.-D. Xiang, *Appl. Phys. Lett.* **71**, 1872 (1997).

⁹ A. Imtiaz, T. M. Wallis, S.-H. Lim, *et al.*, *J. Appl. Phys.* **111**, 093727 (2012).

¹⁰ G. Gramse, M. Kasper, L. Fumagalli, G. Gomila, P. Hinterdorfer, and F. Kienberger, *Nanotechnol.* **25** 145703 (2014).

¹¹ S.-S. Tuca, M. Kasper, F. Kienberger, and G. Gramse, *IEEE Trans. Nanotechnol.* **16**, 991 (2017).

¹² M. C. Biagi, G. Badino, R. Fabregas, G. Gramse, L. Fumagallie, and G. Gomila, *Phys. Chem. Chem. Phys.* **19**, 3884 (2017).

¹³ C. J. Chen *Introduction to Scanning Tunneling Microscopy*, Oxford University Press (1993).

¹⁴ S. Müllegger, S. Tebi, A. K. Das, W. Schöfberger, F. Faschinger, and R. Koch, *Phys. Rev. Lett.* **113**, 133001 (2014).

¹⁵ S. Baumann, W. Paul, T. Choi, C. P. Lutz, A. Ardavan, and A. J. Heinrich *Science* **350**, 417 (2015).

¹⁶ V. Stetsovych, S. Feigl, R. Vranik, *et al.*, *Sci. Rep.* **12**, 2865 (2022).

¹⁷ D. M. Pozar, *Microwave Engineering*, John Wiley & Sons Ltd (2011)

¹⁸ F. Kremer, A. Schönhals, *Broadband Dielectric Spectroscopy*, Springer (2002)

¹⁹ S. M. Anlage, V.V. Talanov, and A. R. Schwartz *Scanning Probe Microscopy: Electrical and Electromechanical Phenomena at the Nanoscale* ed S. V. Kalinin and A. Gruverman, Springer (2006).

²⁰ *Applying Error Correction to Network Analyzer Measurements*, Application Note, Keysight Technologies, Santa Clara, CA (2022). Retrieved from Keysight website: <https://www.keysight.com/us/en/assets/7018-06761/application-notes/5965-7709.pdf>

²¹ S. Feigl, R. Vranik, B. Wit, and S. Müllegger, *Rev. Sci Instr.* **92**, 043710 (2021).

²² B. Wit, R. Vranik, and S. Müllegger, *Sci. Rep.* **12**, 6183 (2022).

²³ T. Brandes, D. Weinmann, and B. Kramer, *Europhys. Lett.* **22**, 51 (1993).

²⁴ G. Goppert and H. Grabert, *C. R. Acad. Sci. Ser. II* **327**, 885 (1999).